Insights into the reionization epoch from cosmic-noon-CIV emitters in the VANDELS survey

S. Mascia[1,2], L. Pentericci[1], A. Saxena[3,4], D. Belfiori[1], A. Calabrò[1], M. Castellano[1], A. Saldana-Lopez[7], M. Talia[5], R. Amorín[8,9], F. Cullen[10], B. Garilli[11], L. Guaita[12], M. LLerena[9], R. J. McLure[10], M. Moresco[6], P. Santini[1], and D. Schaerer[7]

1. INAF – Osservatorio Astronomico di Roma, Via Frascati 33, 00078 Monteporzio Catone, Italy
   e-mail: sara.mascia@inaf.it
2. Dipartimento di Fisica, Università di Roma Tor Vergata, Via della Ricerca Scientifica 1, 00133 Roma, Italy
3. Sub-department of Astrophysics, University of Oxford, Keble Road, Oxford OX1 3RH, UK
4. Department of Physics and Astronomy, University College London, Gower Street, London WC1E 6BT, UK
5. University of Bologna – Department of Physics and Astronomy "Augusto Righi" (DIFA), Via Gobetti 93/2, 40129 Bologna, Italy
6. INAF – Osservatorio Astronomico di Bologna, Via P. Gobetti 93/3, 40129 Bologna, Italy
7. Department of Astronomy, University of Geneva, 51 Chemin Pegasi, 1290 Versoix, Switzerland
8. Instituto de Investigación Multidisciplinar en Ciencia y Tecnología, Universidad de La Serena, Raúl Bitràn 1305, La Serena, Chile
9. Departamento de Física y Astronomía, Universidad de La Serena, Av. Juan Cisternas 1200 Norte, La Serena, Chile
10. SUPAScottish Universities Physics Alliance, Institute for Astronomy, University of Edinburgh, Royal Observatory, Edinburgh EH9 3HJ, UK
11. INAF-IASF Milano, Via Alfonso Corti 12, 20133 Milano, Italy
12. Departamento de Ciencias Fisicas, Facultad de Ciencias Exactas, Universidad Andres Bello, Fernandez Concha 700, Las Condes, Santiago, Chile

ABSTRACT

Recently, intense emission from nebular CIII] and CIV emission lines have been observed in galaxies in the epoch of reionization ($z > 6$) and have been proposed as the prime way of measuring their redshift and studying their stellar populations. These galaxies might represent the best examples of cosmic reionizers, as suggested by recent low-z observations of Lyman continuum emitting galaxies, but it is hard to directly study the production and escape of ionizing photons at such high redshifts. The ESO spectroscopic public survey VANDELS offers the unique opportunity to find rare examples of such galaxies at cosmic noon ($z \sim 3$), thanks to the ultra deep observations available. We have selected a sample of 39 galaxies showing CIV emission, whose origin (after a careful comparison to photoionization models) can be ascribed to star formation and not to active galactic nuclei. By using a multiwavelength approach, we determined their physical properties including metallicity and the ionization parameter and compared them to the properties of the parent population to understand what the ingredients are that could characterize the analogs of the cosmic reionizers. We find that CIV emitters are galaxies with high photon production efficiency and there are strong indications that they might also have a large escape fraction: given the visibility of CIV in the epoch of reionization, this could become the best tool to pinpoint the cosmic reioinzers.

Key words. Galaxy: evolution – galaxies: high-redshift – galaxies: formation – galaxies: ISM – galaxies: general

1. Introduction

The rest-frame UV and optical emission lines that emerge from star-forming (SF) galaxies are an important indicator of the nature and strength of the ionizing radiation and the conditions in the interstellar medium (ISM) since they can be used to infer gas-phase abundances and ionization parameters. Particularly the rest-UV range is currently fundamental to study the early galaxies in the epoch of reionization (EoR), as it is accessible with ground-based telescopes and now with the JWST (Robertson 2022). In the last few years, prominent high-ionization nebular emission lines such as OIII] $\lambda\lambda$ 1661,1666, CIV $\lambda\lambda$ 1548,1551 (hereafter simply CIV λ 1550), HeII λ 1640, and CIII] λ 1907 + CIII] λ 1909 (hereafter simply CIII] λ 1910) have been observed in a few $z \simeq 6$–7 galaxies (Stark et al. 2015; Mainali et al. 2018), indicating that these systems are characterized by extreme radiation fields. Whether such properties are really common or

not at these early epochs is still a matter of debate (e.g. see Castellano et al. 2022), but they might become the best probes to detect and characterize the most distant sources, since at $z > 7$ the Lyα emission line, which is usually the strongest line in young SF galaxies, starts to be suppressed by the increasingly neutral intergalactic medium (IGM) as we approach the reionization epoch (Pentericci et al. 2018b; Jung et al. 2020; Ouchi et al. 2020; Bolan et al. 2022).

The nebular CIV emission line, requiring comparably high ionization energies as the HeII line ($E > 47.9$ eV and > 54.4 eV, respectively), has recently attracted attention since it has been shown that its presence might be strongly linked to the escape of Lyman continuum (LyC) photons from galaxies. Indeed Schaerer et al. (2022) recently detected CIV in several confirmed LyC leakers at $z < 0.7$, finding CIV emission in all LyC emitters with escape fractions $f_{esc} > 0.1$ and suggesting that such strong leakers have CIV/CIII ratios above ~0.75. This

makes the CIV emission line a very promising indirect tracer of LyC f_{esc}.

Other observations also support this scenario: one of the few solid LyC leakers at high redshift, Ion2 at $z = 3.2$, shows the presence of nebular emission in both CIV and CIII], with a rather high ratio CIV/CIII] from deep X-shooter spectroscopy (Vanzella et al. 2020). Naidu et al. (2022) indirectly classified $z \sim 2$ LAEs into strong LyC leaking and non leaking galaxies based on the shape and peak separation of their Lyα profile. The composite spectrum of the potential LyC emitters shows narrow CIV as well as HeII, while there is no sign of these lines in the analogous stack of the non leakers (see also Saldana-Lopez et al. 2022a). If confirmed this link would be really important to probe cosmic reionization: at $z > 5$, directly detecting the LyC photons escaping from galaxies is impossible because of the IGM opacity (Inoue et al. 2014). We therefore need indirect indicators, that is to say observational properties that correlate with f_{esc} and can be observed in the EoR. Many such indirect diagnostics have been proposed (e.g., Verhamme et al. 2017; Izotov et al. 2018; Marchi et al. 2018), but all still present a large scatter (see Flury et al. 2022a, for a recent comprehensive study on low redshift LyC diagnostics).

To better interpret this intriguing link between nebular emission and the production and escape of ionizing photons, and the important consequences it could have for reionization, detailed investigations need to be conducted at low and intermediate redshift. However, nebular CIV emission is extremely rare in normal SF galaxies at least at low and intermediate redshift. Berg et al. (2019) detected CIV and HeII in two nearby SF galaxies and propose that this combination of emission may identify galaxies that produce and transmit a substantial number of high-energy photons contributing to cosmic reionization. Senchyna et al. (2022) also found that both nebular CIV and HeII appear in nearby lower metallicity galaxies (<0.1 $Z_\odot$), provided the specific star formation rate (sSFR) is large enough to guarantee a significant population of high-mass stars, although the equivalent widths (EWs) appear smaller than those measured in individual systems at $z > 6$. At intermediate redshift ($z \sim 2-3$), although a hint of CIV emission appears in deep stacked spectra of SF galaxies, especially when combining a subsample of galaxies with Lyα in emission (Shapley et al. 2003; Pahl et al. 2021), individual detections are very rare. Tang et al. (2021) investigated a large sample of more than 100 extreme emission line galaxies, selected to have strong OIII, and detected CIV emission in only five sources, but with EWs up to 25 Å. Similarly, at $z \sim 2$, Du et al. (2020) analyzed a large sample of possible analogs of EoR sources but only found two objects with strong rest-UV metal line emission including significant CIV which appear comparable to the $z > 6.5$ galaxies. Only in low-mass galaxies, which are mostly observable thanks to lensing magnification (Vanzella et al. 2016, 2020, 2021; Mainali et al. 2017), does there seem to be a somewhat higher fraction of sources showing prominent UV emission lines, with the most extreme CIII] emitters also showing nebular CIV emission with rest EWs 3–8 Å (Stark et al. 2015; LLerena et al. 2022). These galaxies show very large sSFRs, indicating that they are in a period of rapid stellar mass growth and have very blue continuum UV slopes, indicating minimal dust content, young ages, and low metallicity (Amorín et al. 2017).

In this context, the VANDELS survey (McLure et al. 2018; Pentericci et al. 2018a) provides the ideal database to search for galaxies showing the rare and faint CIV nebular emission line, since it provides some of the deepest spectra of intermediate redshift SF galaxies available to date. In particular VANDELS

spectra can identify this emission line in galaxies in a redshift range ($\sim 3-4$) where also the direct detection of LyC flux is possible and thus a confirmation of the link between LyC escape and CIV emission can be directly tested. With this aim we have thus searched for a sub-sample of galaxies at $z \sim 2.5-5$ that show strong nebular CIV emission from the VANDELS survey, in order to determine their physical proprieties and identify their nature as possible analogs of the cosmic reionizers.

The paper is structured as follows. The selection criteria and the sample of CIV emitters in the VANDELS survey are discussed in Sect. 2. Section 3 examines their spectroscopic properties, while Sect. 4 analyzes the emission lines' properties to distinguish SF galaxies from Active Galactic Nuclei (AGNs) in our sample. In Sect. 5 we investigate the physical properties of the SF CIV emitters and in Sect. 6 we investigate how these properties are linked with cosmic reionization physical components. Finally, we summarize our findings in Sect. 7.

Throughout this paper, we assume a flat ΛCDM cosmology with $H_0 = 67.7$ km s^{-1} Mpc^{-1} and $\Omega_m = 0.307$ (Planck Collaboration XIII 2016). All magnitudes are expressed in the AB system (Oke & Gunn 1983).

2. The VANDELS CIV emitters

2.1. Sample selection

For our analysis we have used data from "VANDELS: a VIMOS survey of the CDFS and UDS fields", which is a recently completed ESO public spectroscopic survey carried out using the VIMOS spectrograph on the Very Large Telescope (VLT). VANDELS targets are selected in the UKIDSS Ultra Deep Survey (UDS; RA = 2:18, Dec = −5:10), and the *Chandra* Deep Field South (CDFS; RA = 3:32, Dec = −27:48): VANDELS footprints are centered on the HST areas observed by the CANDELS program (Grogin et al. 2011; Koekemoer et al. 2011), although given the VIMOS field of view, they are larger. The survey description and initial target selection strategies can be found in McLure et al. (2018), while data reduction and redshift determination methods can be found in Pentericci et al. (2018a). Here we give a brief description of the most important aspects relevant to this work.

VANDELS targeted SF galaxies at $z > 2.4$ as well as massive, passive galaxies in the redshift range $1 < z < 2.5$, with integration times ranging from 20 to 80 hours depending on the magnitude to ensure a uniform signal-to-noise ratio (S/N) on the continuum, with most targets observed for 40 hours or more. The EASYLIFE data reduction pipeline was used to reduce the spectra (Garilli et al. 2012), producing the extracted 1D spectra, resampled 2D spectra, and sky-subtracted spectra. Spectroscopic redshifts were derived using the pandora.ez tool (Garilli et al. 2010) by cross-correlation with galaxy templates. The reliability of the redshifts is quantified with a quality flag (QF) as follows: 0 means no redshift could be determined; 1, 2, 3 and 4 mean respectively a probability of 50%, 75%, 95% and 100% of the redshift being correct; finally 9 means that the spectrum shows a single emission line. The redshift measurement accuracy of spectroscopic observations is typically 150 km s^{-1}. For more information, see Pentericci et al. (2018a) for details on data reduction and redshift determination.

In this work we have used galaxies from the fourth and final data release (DR4) which is described in Garilli et al. (2021). The data release contains spectra of approximately 2100 galaxies in the redshift range of $1.0 < z < 7.0$, with over 70% of the targets having at least 40 h of on-source integration time.

2.2. Identification of CIV emitters

We base our work on the official VANDELS emission line catalog which will be presented in Talia & Schreiber (2023). Specifically, we use the catalog that was build using Gaussian fit measurements performed with `slinefit`[1] (Schreiber et al. 2018), an automated code that models the observed spectrum of a galaxy as a combination of a stellar continuum model and a set of emission and absorption lines. A set of templates is linearly combined to best fit the continuum. The templates were built with the Bruzual & Charlot (2003) stellar population models and fit to the EAzY (Brammer et al. 2008) default template set using FAST (Kriek et al. 2009). The code searches for lines around their expected locations given by the VANDELS official redshift. Each line with a S/N higher than 3 is allowed its own offset, with a maximum value set by ± 1000 km s^{-1} while lines with a lower S/N are instead fixed at their expected position. Therefore, for each detected line, the catalog is formed with the following information: flux and error, rest-frame equivalent width (EW$_0$) and error, and the rest-frame full width at half maximum (FWHM) with error. By using the Monte Carlo technique, these errors are determined by randomly perturbing the galaxy spectrum based on its error spectrum, and then computing the uncertainties from the standard deviation of these perturbations compared to the original data.

For our analysis we selected galaxies with a reliability flag 3, 4 and 9, which show a CIV emission line with a S/N greater than 2.5. To ensure the reliability of the lowest S/N detections and following (Saxena et al. 2020) we produced a stacked spectrum of the 12 sources with $2.5 \leq S/N \leq 3$, as an additional check to ensure that they are indeed bona fide CIV emitters (see also Sect. 4.4). In this way we verified that we can safely consider these sources in the sample. We selected a total of 50 galaxies.

From this list generated by the automatic procedure we removed by eye six sources which present clear problems of sky-residuals in the region of the CIV emission and one source with evidence of merger in the spectrum. Finally from a visual inspection of all VANDELS QF 3, 4 and 9 sources we note that the official catalog failed to detect some galaxies with clear CIV emission lines which were not correctly identified by `slinefit`. This is probably due to the limited velocity offset allowed in the automatic search and to the fact that the reference redshift used for the search is the "VANDELS redshift", which is not the systemic redshift but is in general driven by the strongest features present in the spectrum. In few cases this redshift is closer to the Lyα redshift or to the ISM redshift depending on their relative strength. A further 8 sources were identified and reanalyzed through `slinefit` by correctly calibrating the redshift (on the CIII] line when possible) which represents better the systemic redshift of the galaxies.

2.3. Removal of X-ray AGN/BLAGN and final sample

Since we want to study the nature of CIV in SF galaxies, we excluded the sources which are obvious AGN: in particular we excluded 8 X-ray detected sources from the CDFS 7 Ms Source Catalogs (Luo et al. 2017) and the UDS X-ray observations (Kocevski et al. 2018), of which 4 are broad line AGNs (BLAGNs: CDFS003360, CDFS019824, UDS017629 and UDS199159) which are easy to recognize from the broad UV emission line, and 4 narrow line AGNs (NLAGNs: CDFS005827, CDFS019505, UDS025482 and UDS018960).

For an individual analysis of these sources see Bongiorno et al. (in prep.).

In conclusion, from the parent sample made of 933 galaxies at $2.5 \leq z \leq 5$ without the AGN contribution, we obtain a subsample of 43 sources, 20 from the UDS field, and 23 from the CDFS field. The IDs, RA and DEC coordinates, redshifts, related flags and emission line information are presented in Table 1. This sample might still contain some NLAGNs with no X-ray counterpart. In the following section, we refine our analysis and employ emission line ratio diagrams to obtain a sample of purely SF CIV galaxies.

In Fig. 1 we show the distribution of the galaxies' H_{AB} magnitude as a function of the redshift for the CIV sample (highlighted in purple) and the parent sample (gray symbols), i.e., all other VANDELS sources after removing the AGNs, as classified in Bongiorno et al. (in prep.). For this comparison the parent sample has been cut between redshift 2.5 and 5. As we can see the CIV emitters are a representative subset of the VANDELS population at least in terms of H-band and redshift distribution.

3. Spectroscopic properties of the CIV emitters

In Fig. 2 we present the distribution of the rest-frame equivalent widths (EW$_0$s) of the CIV emission line in our sample, which range from 1 to 29 Å. Therefore, although most objects show EW$_0$ of a few Å, in the VANDELS dataset we also find some galaxies with extreme EWs, analogous to those found in the epoch of reionization (Stark et al. 2014; Mainali et al. 2018). In Table 1 we report the fluxes of the CIV lines and their EW$_0$s. We also present the fluxes for the HeII, OIII] and CIII] emission lines from the catalog of Talia & Schreiber (2023) plus the 8 additional sources considered in this work. We then analyze the relation between the CIV emission line and the other UV lines and we present the results in Fig. 3, where we plot as limits all lines detected with a S/N lower than 2.5. We see a good correlation in all cases. In the insets of Fig. 3 we also indicate, for each distribution, the probability r_K that the two variables are dependent, following the generalized Kendall's τ statistic including the upper limits (Isobe et al. 1986). Other studies at similarly high redshift have investigated analogous relations between UV lines, although only focusing on the CIII] emission line: for example Schmidt et al. (2021) report that the strengths of HeII, OIII, and SiIII correlate with the flux of the CIII] emission while Marchi et al. (2019), Cullen et al. (2019) found that that the Lyα EW and the CIII] EW are strongly related (see also Stark et al. 2014) although this relation has a really large scatter (e.g., Le Fèvre et al. 2019) and therefore it appears strong only when using stacks.

Even if our emission lines are all quite close in wavelength, to perform a quantitative analysis, dust reddening should be consider. Due to the lack of direct measurements of Hα and Hβ, we used the SED fitting results (see Sect. 5.1) to estimate the amount of corrections for dust attenuation. From the stellar A_v (SED) we computed the stellar reddening $E(B - V)$ and then the nebular $E(B - V)$ (following Calzetti et al. 2000): this quantity is on average 0.11. These results are consistent with those reported by Saxena et al. (2022a), in which a $E(B - V)_{\text{nebular}} \sim 0$ was obtained analyzing the stack of the brightest sub-sample of the VANDELS CIV emitters presented in this work. Since the dust correction inferred would only marginally affect our line ratios, we present only observed values.

For the CIV emission we must also consider a correction for a component due to stellar emission. Stellar CIV produces a classical p-Cygni profile, that is present only in a small subset of

---

[1] https://github.com/cschreib/slinefit

Table 1. Main features of the CIV emitters.

ID	Dec [J2000]	RA [J2000]	z	AGN	HeII	CIII]	OIII]	CIV	EW$_0$ [Å]
CDFS 000303	−27.937461	53.069643	3.6137	×	<0.6	1.2 ± 0.3	<1.2	1.0 ± 0.2	3.7 ± 0.9
CDFS 003839	−27.875749	53.144602	3.458	✓	1.6 ± 0.6	<1.2	<2.2	3.4 ± 0.8	14 ± 3
CDFS 006327	−27.850722	53.178278	3.4937	✓	1.4 ± 0.4	1.0 ± 0.4	<0.6	1.7 ± 0.4	7.8 ± 1.7
CDFS 012637	−27.795843	53.122588	3.4655	?	<0.8	1.3 ± 0.4	<1.8	1.6 ± 0.5	6 ± 2
CDFS 014277	−27.785081	53.231559	3.3616	×	<1.2	4.4 ± 1.5	<1.8	5.9 ± 0.7	9.8 ± 1.3
CDFS 021733	−27.724985	53.055324	3.1087	×	<1.7	<3	<1.9	6.2 ± 1.4	29 ± 8
CDFS 021776	−27.724619	53.098507	4.741	×	<2.0	−	<4.0	2.6 ± 0.8	13 ± 5
CDFS 025178	−27.689563	53.184370	2.806	?	<1.4	<1.6	<1.9	4.4 ± 0.9	5.1 ± 1.0
CDFS 025760	−27.696507	53.069094	4.79	×	92 ± 5	−	67 ± 14	32 ± 3	20 ± 2
CDFS 028933	−27.848752	53.029622	3.7795	×	<1.0	1.9 ± 0.3	<1.0	2.2 ± 0.2	9.4 ± 1.0
CDFS 029763	−27.825989	53.238443	3.105	?	<0.4	<0.5	0.8 ± 0.2	0.7 ± 0.3	8 ± 3
CDFS 032490	−27.754031	53.219545	3.0747	?	<0.6	1.1 ± 0.4	<0.4	1.1 ± 0.4	9 ± 3
CDFS 128455	−27.745586	53.003635	3.4813	×	<1.5	3.9 ± 1.2	<2.1	7 ± 3	3.5 ± 1.4
CDFS 202937	−27.963161	53.218947	3.735	✓	4.2 ± 0.6	3.1 ± 0.8	<2.1	4.3 ± 0.6	8.9 ± 1.3
CDFS 203861	−27.956412	53.215551	4.7502	×	<5.0	−	<3.8	5.0 ± 1.7	19 ± 7
CDFS 203989	−27.955446	53.019099	3.1366	×	1.4 ± 0.4	4.1 ± 0.5	1.8 ± 0.3	4.5 ± 0.7	8.8 ± 1.4
CDFS 208175	−27.923411	53.266337	3.462	?	<1.4	1.1 ± 0.4	<1.8	3.6 ± 1.2	3.8 ± 1.3
CDFS 209144	−27.916473	53.070682	4.4286	×	<2.0	−	<1.9	2.5 ± 0.9	8 ± 3.1
CDFS 212043	−27.894033	52.994478	3.395	×	<1.6	4.2 ± 0.8	<1.4	2.9 ± 0.9	3.4 ± 1.1
CDFS 231741	−27.747690	53.287112	4.0068	×	<0.9	3.6 ± 1.2	2.8 ± 0.6	2.9 ± 0.7	6.3 ± 1.4
CDFS 247279	−27.676973	53.206236	3.2959	×	<1.8	4.0 ± 0.6	<2.6	4.3 ± 0.8	7.4 ± 1.5
CDFS 009384★	−27.823526	53.078521	3.5480	×	0.8 ± 0.2	<1.6	<1.5	0.33 ± 0.11	1.1 ± 0.4
CDFS 025002★	−27.688314	53.066713	3.7915	?	<1.6	1.7 ± 0.8	<19	1.9 ± 0.5	4.4 ± 1.3
UDS 000184	−5.275796	34.489558	4.3722	×	<2.7	<15	6.6 ± 1.1	6.5 ± 1.3	10 ± 2
UDS 003724	−5.255394	34.395118	3.4616	×	<1.3	3.8 ± 0.9	<4.4	4.5 ± 0.7	7.6 ± 1.2
UDS 018872	−5.171582	34.371472	4.8799	×	<3.7	−	<5.4	3.3 ± 1.1	10 ± 4
UDS 020394	−5.163315	34.535879	3.3018	×	<1.1	3.9 ± 0.4	<5.0	2.5 ± 0.8	5.1 ± 1.6
UDS 021234	−5.158691	34.420972	4.6008	×	2.2 ± 0.6	−	<15	5.7 ± 1.0	17 ± 4
UDS 021291	−5.158290	34.295009	3.625	×	<0.9	2.6 ± 1.0	<1.3	1.9 ± 0.6	5.5 ± 1.9
UDS 033733	−5.162411	34.406837	3.1424	×	<0.8	<1.5	<0.6	1.4 ± 0.5	12 ± 5
UDS 034251	−5.153870	34.581079	3.61	?	<1.3	<1.6	<1.4	2.1 ± 0.8	6 ± 2
UDS 034333	−5.152631	34.404969	3.927	×	<0.8	<2.1	<2.0	2.5 ± 0.6	14 ± 4
UDS 145830	−5.336489	34.556466	3.2094	✓	8.3 ± 1.0	3.5 ± 1.2	<3.4	5.5 ± 1.3	18 ± 6
UDS 283510	−5.368315	34.388651	4.5092	×	<2.7	−	<3.7	5.3 ± 1.1	18 ± 5
UDS 313619	−5.287081	34.242560	3.188	×	<2.4	10.7 ± 1.8	4.6 ± 1.7	6.6 ± 1.9	7 ± 2
UDS 379641	−5.110200	34.334556	4.1161	×	<1.8	<4.7	<3.5	2.9 ± 1.0	9 ± 3
UDS 395442	−5.070635	34.434154	3.589	×	<1.3	<2.5	<1.1	2.6 ± 0.9	2.3 ± 0.8
UDS 020932★	−5.160535	34.518914	3.6005	×	<2.4	<10	<3.1	3.2 ± 0.9	3.5 ± 1.0
UDS 140603★	−5.361135	34.393002	3.4146	?	<3.0	<4.2	<3.0	5.0 ± 1.0	5.6 ± 1.2
UDS 152744★	−5.303281	34.393005	2.7243	?	<3.2	<1.9	<2.4	5.2 ± 1.1	2.4 ± 0.5
UDS 312746★	−5.289354	34.243205	3.5207	×	<2.1	<6.8	<5.4	2.2 ± 0.7	3.2 ± 1.1
UDS 315235★	−5.282526	34.473701	3.5976	×	<2.4	<4.1	<4.4	1.8 ± 0.6	2.6 ± 0.9
UDS 388069★	−5.089615	34.339181	3.4550	?	<1.7	<2.0	<1.1	2.3 ± 0.4	3.7 ± 0.7

Notes. AGN indicates the nature of the sources: ✓ for X-ray/BLAGN, ? for a possible AGN and × for a purely SF galaxy. The measured HeII, CIII], OIII] and CIV rest-frame line fluxes are in units of $\times 10^{-18}$ erg s^{-1} cm^{-2}, and the EW$_0$ of the CIV line is un units of Å. The sources with the asterisk are the ones reanalyzed with `slinefit` and not contained in Talia & Schreiber (2023). The sources in red are the best candidates to be strong LyC leakers (as discussed in Sect. 6).

our sources. We consider the results of Saxena et al. (2022a), in which we derived a stellar component to contribute less than 25% on the strong CIV emission[2] by fitting the individual galaxy spectra using SEDs that only contain stellar emission as done in Saldana-Lopez et al. (2022b). As we subsequently show in the next section, the p-Cygni profile is missing in the stacked spectrum of all SF galaxies, again indicating that the stellar compo-

nent is probably very small on average in the total sample and possibly present only in the stronger emitters. In the following analysis, we use the uncorrected CIV, but we indicate in the various cases if and how this correction could alter our results.

4. Classification of SF and AGN based on UV emission lines

None of the 43 sources in our sample have X-ray individual detections: however some of them might still be faint AGN. In

---

[2] We note that given our limited resolution and the fact that the stellar component (both emission and absorption) is broad, this might be an overestimate.
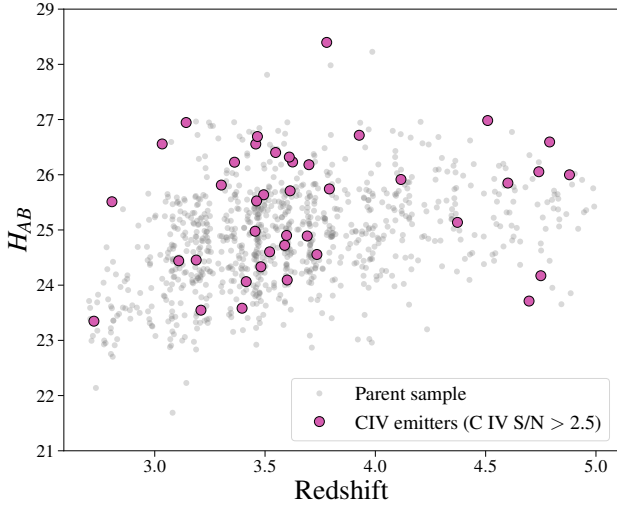
Fig. 1. Distribution of H_{AB} of the CIV emitters with redshift. The sources cover a redshift range of $2.8 < z < 5$, with a median redshift of $\bar{z} \sim 3.54$. Of the 43 selected sources, 3 of them do not show any detection in the H (HST/$F160W$) band, so they are not shown in the figure.
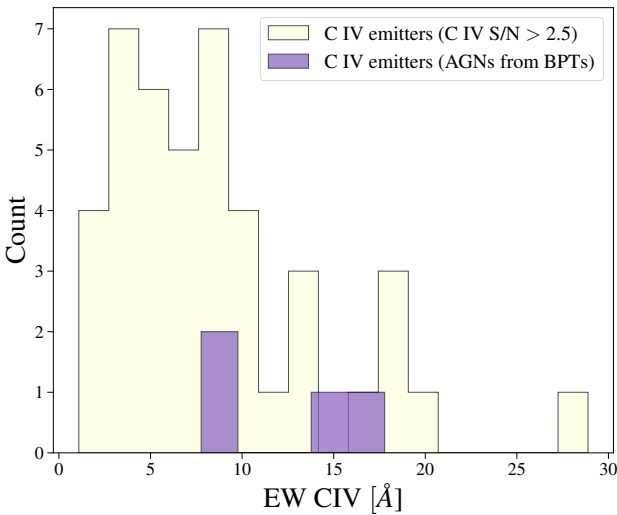
Fig. 2. Light distribution: measured EW_0 of the CIV emission line for the CIV emitters ($S/N > 2.5$) identified in both CDFS and UDS fields. Purple distribution: measured EW_0 of the CIV emission line for the sample of certain AGNs described in Sect. 4.3.

order to identify only the population of SF galaxies, we compare the UV emission properties of our sources to the predictions of photoionization models of AGN and SF galaxies. At variance with the seminal work by Baldwin et al. (1981) who first produced diagrams to discriminate AGN from SF galaxies, we use UV emission lines instead of those falling in the optical rest frame.

Specifically we consider the CIV, HeII and CIII] (we do not include the OIII emission since it is only detected in few galaxies). Indeed, these lines are among the most commonly detected UV emission lines in galaxy spectra and they are used to discriminate between photoionization by AGN and shocks in galaxies as well as to investigate the ISM metallicity. The CIV/HeII or CIII]/HeII ratios are sensitive to metallicity, while CIII]/CIV depends mostly on the ionization parameter (e.g., Groves et al. 2004; Nagao et al. 2006; Nanayakkara et al. 2019). As we dis-

cuss in the next sections, the models of AGN and SF galaxies occupy two distinct regions in the UV diagnostic diagrams (henceforth also called UV-BPTs for simplicity), so these can be used as discriminators to effectively classify our sources.

4.1. AGN models: *Feltre et al. (2016)*

The models developed by Feltre et al. (2016) for the emission by the AGN narrow-line regions have been created using CLOUDY (Ferland et al. 2013)[3]. They consider a parameterization of the gas distribution as a cloud of a single type but contaminated by dust and dominated by the radiation pressure. It is useful to highlight that in these models, the line measurements are not corrected for dust attenuation.

For the purposes of our analysis, we use models with $Z = 0.0001, 0.0002, 0.0005, 0.001, 0.002, 0.004, 0.006, 0.02$ and 0.04 with no priors on n_H in order to identify a clear AGN region in all the UV-BPTs. These models were constructed using the relative abundances of heavy elements for solar metallicity (Caffau et al. 2011). The predicted intensities of 20 optical and ultraviolet emission lines are then produced (in units of erg s^{-1}). We consider the CIV, HeII and CIII] predicted intensities. Since we also want to produce a diagnostic diagram of CIV EW with CIV/HeII which was already used by (Nakajima et al. 2018b), we need to also derive the EW of the CIV line from the luminosities provided by the models. To determine the line continuum we followed the procedure outlined in Castellano et al. (2022). We first renormalize the incident spectra to a chosen fraction of the observed average flux in the R band, i.e., 5950–7250 Å, which corresponds to the observable non ionizing UV flux at ~1500 Å, and then compute the EW of the CIV line on the basis of the predicted line flux for each model and of the observed flux at the relevant wavelength.

### 4.2. SF models: *Gutkin et al. (2016)* and *Xiao et al. (2018)*

It has been argued that the inclusion of interacting binary stars in stellar population synthesis models may hold the key to explain the observations of bright high ionization nebular emission lines in the spectra of high redshift SF galaxies (Stanway et al. 2016; Eldridge et al. 2017). Xiao et al. (2018) combine the output of the stellar spectral synthesis model BPASS (Binary Population and Spectral Synthesis) used in conjunction with the photoionization code CLOUD to predict the nebular emission from HII regions around young stellar populations over a range of compositions and ages.

In total, there are 80 262 photoionization models, including separate models for binary and single stars[4]. For our analysis, we consider the photoionization models for binary stars with $Z = 0.001, 0.002, 0.02$ and $\log(Age/yr) = 6, 6.5, 7, 7.5$. For each model, the predicted luminosities and EWs of 17 optical and ultraviolet emission-lines are given (in units of erg s^{-1} and Å, respectively). We retrieved the CIV, HeII and CIII] predicted intensities and EWs.

In addition, we also consider the models developed by Gutkin et al. (2016) for the nebular emission from SF galaxies. They have been created using CLOUD (Ferland et al. 2013). For our analysis, we use models with $Z = 0.0001, 0.0002, 0.001, 0.002$ and 0.02 with no priors on n_H and with relative elemental

---

[3] These models can be found at `http://www.iap.fr/neogal/agn-models.html`

[4] These models can be found at `https://bpass.auckland.ac.nz/4.html`
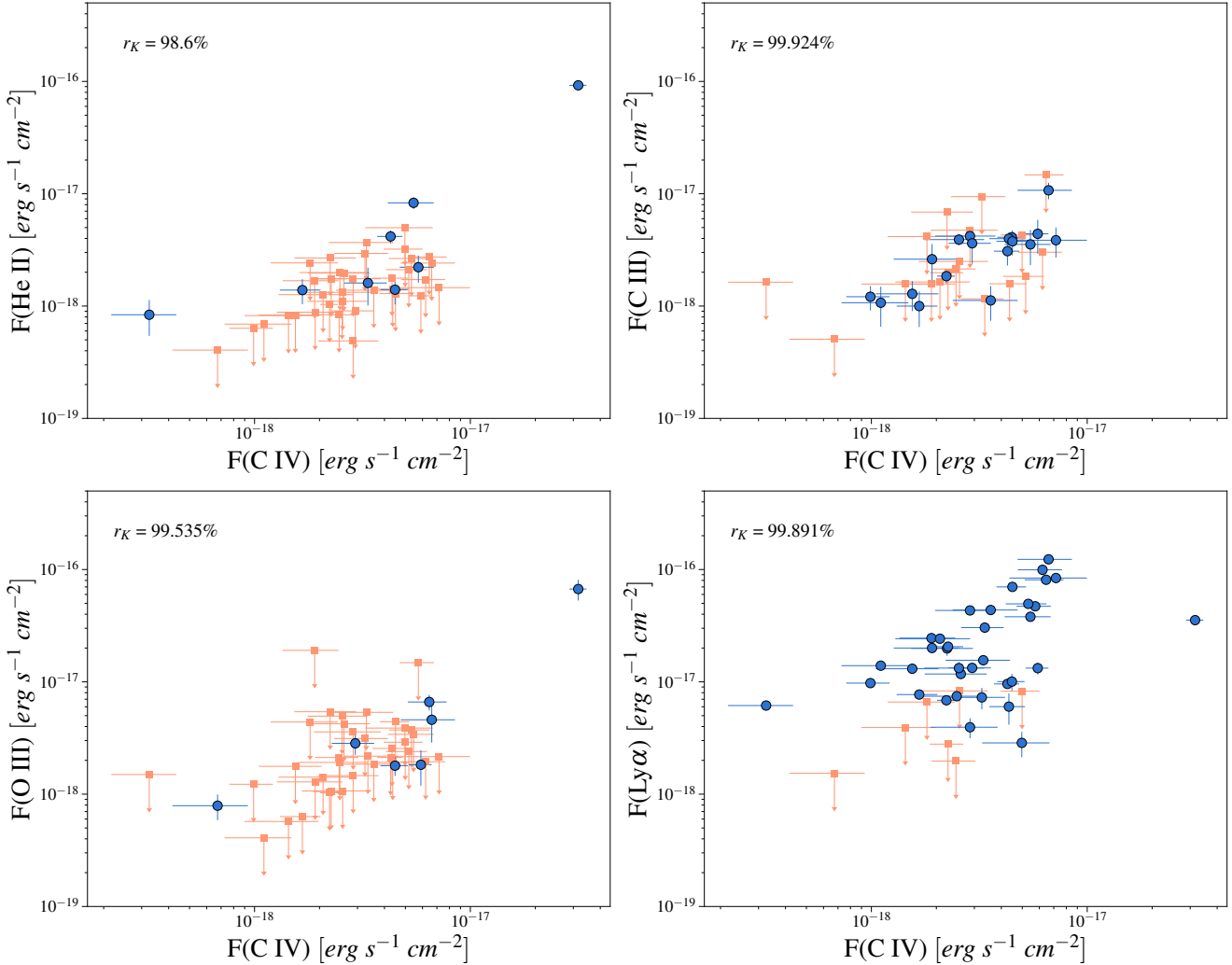
Fig. 3. Distribution of the measured HeII, CIII], OIII] and Lyα line fluxes and the CIV line flux for the selected CIV emitters ($S/N > 2.5$) identified in both CDFS and UDS fields (blue points). If S/N of a line is lower than 2.5, we set $2|\sigma|$ as upper limit (orange squares). In the figure it is also reported the correlation coefficient r_K from the generalized Kendall's τ statistic.

abundances fixed at Solar ratios (Caffau et al. 2011). The predicted intensities of 20 optical and ultraviolet emission-lines are then produced (in units of erg s^{-1})[5]. As in the previous cases, we consider the CIV, HeII and CIII] predicted intensities.

Similarly to what done with the Feltre et al. (2016) models, we derive also the EW of the CIV line from the luminosities provided by the models, employing the method described in Sect. 4.1 and in Castellano et al. (2022).

4.3. Separating SF galaxies from AGN in the UV-BPTs

We now compare the properties of our sample of CIV emitters with the predictions from photoionization models for nebular emission from SF galaxies or AGN narrow-line regions described in the previous sections. Following the original diagnostics proposed by Feltre et al. (2016) we shall study the two relations CIII]/HeII vs. CIV/HeII and CIV/HeII vs. CIV/CIII]. In addition to these, and following the work by Nakajima et al. (2018b), who constructed photoionization models to interpret the UV spectra of CIII emitters selected from the VUDS sur-

vey at $z = 2-4$, we also use the relation CIV/CIII] versus (CIII]+CIV)/HeII, and CIV EW vs. CIV/HeII.

In Fig. 4 we present the four different diagrams, which for simplicity we refer to UV-BPT1, UV-BPT2, UV-BPT3 and UV-BPT4 from here on. These diagrams give the advantage that objects can be tracked and diagnosed even if only one of the three lines is detected – in fact, if the S/N of a line is <2 we consider $2|\sigma|$ as a limit. Whenever both lines considered in a certain line ratio are not detected but are both limits, we do not plot that object in the relevant UV-BPT diagram. This means that only UV-BPT3 and UV-BPT4 contain all the 43 objects in our sample.

In each diagram, the dots with error bars and/or limits indicate the position of the sources in our sample; the green triangles represent the position of the X-ray AGNs which have been excluded from our catalog and the green and magenta dots are the predictions from the models described in the previous subsections, respectively from the AGN models (Feltre et al. 2016), and the SF models (Gutkin et al. 2016; Xiao et al. 2018). It can be seen that the models occupy regions that are quite well although not completely separated in each of the UV-BPT diagrams. In the UV-BPT1 and UV-BPT4 diagrams we also plot the separation between AGN and SF galaxies proposed by

---

[5] These models can be found at `http://www.iap.fr/neogal/sf-models.html`
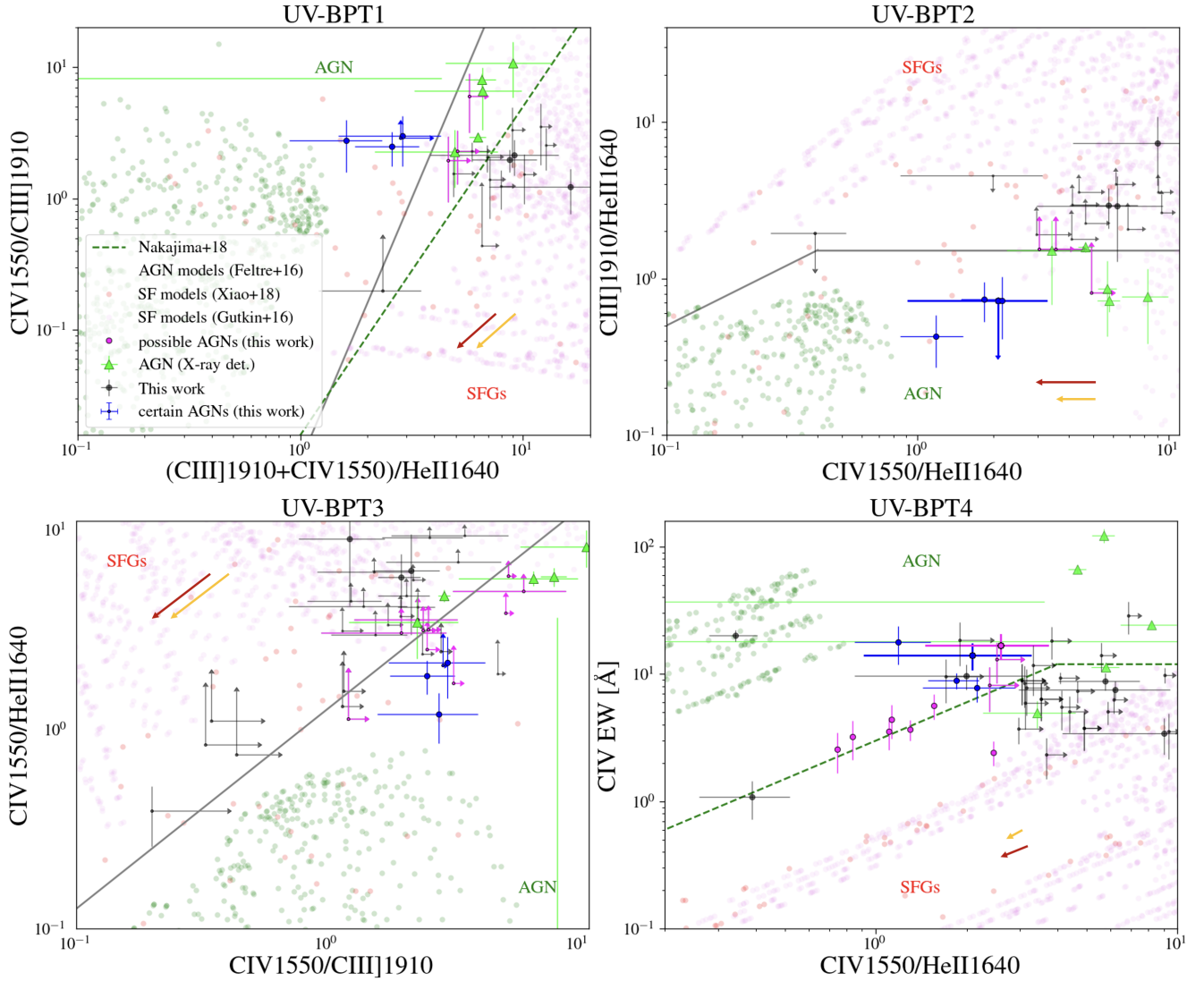
Fig. 4. UV diagnostic diagrams presenting photoionization models of AGN (dark green dots; Feltre et al. 2016) and SF galaxies (SFGs; red dots; Xiao et al. 2018; Gutkin et al. 2016). The separating lines consistently divide the two populations, and thus our sample of CIV emitters in: SF galaxies (black dots), confirmed AGNs (X-ray detected, in green), certain AGNs (blue dots) and possible AGNs (magenta), classified according to our criteria. The dashed green line division between ionization due to star formation alone and ionization due to AGN has been presented in Nakajima et al. (2018b). The grey solid line represents our best guess of the possible division between the two regions in all the UV-BPTs. We also plot two arrows indicating the displacement of the data points by imposing a stellar correction of 20% (red one) and 10% (orange one) for the CIV emission (based on Saxena et al. 2022a).

Nakajima et al. (2018b) using the distributions of galaxies and AGNs observed in the VUDS survey.

Based on the models considered and on the position of the X-ray detected AGN, we proposed a slightly revised version of the separation between AGN and SF galaxies in the UV-BPT1 diagram which can be written as:

$$\log(\text{CIV/CIII}) < 4\log((\text{CIV} + \text{CIII})/\text{HeII}) - 2. \tag{1}$$

For the other UV-BPT diagrams we consider the following separation lines: for UV-BPT2

$$\begin{aligned} \log(\text{CIII}]/\text{HeII}) &< 0.8\log(\text{CIV/HeII}) + 0.5 \ [\log(\text{CIV/HeII}) < 0.4] \\ &< 1.5 \ [\log(\text{CIV/HeII}) \geq 0.4]. \end{aligned} \tag{2}$$

For UV-BPT3 (not considered by Nakajima et al. 2018b):

$$\log(\text{CIV/HeII}) < \log(\text{CIV/CIII}) + 0.1. \tag{3}$$

For UV-BPT4 (same as in Nakajima et al. 2018b),

$$\begin{aligned} \text{CIV EW} &< 3 \times (\text{CIV/HeII}) \ [\text{CIV/HeII} < 4] \\ &< 12 \ [\text{CIV/HeII} \geq 4]. \end{aligned} \tag{4}$$

Not all of the 43 sources are in all the diagrams but, when present, their position is always consistently in the AGN or SF part of the diagrams for all cases apart from UV-BPT4. In fact we note that the results from UV-BPT4 are more ambiguous since most sources, including some of the X-ray detected NLAGNs are located in an intermediate region in between the AGN and SF models. In addition, it seems that none of the SF models, can produce CIV EW as large as those observed in our sample. This problem was already highlighted in Saxena et al. (2020), where we noted that although the low-metallicity binary star models are able to reproduce the UV line ratios of their HeII emitters, they under-predict the HeII EWs. The same applies to the CIV emission which is under-predicted by BPASS, as also discussed

in Nakajima et al. (2018b), Le Fèvre et al. (2019). For the separation between AGN and SF galaxies we therefore base our classification on the bases of the other 3 UV-BPT diagrams. Specifically we find:

- four sources whose position is consistently in the AGN regions in all UV-BPT diagrams: we call these sources "certain AGN" and indicate them with blue dots;
- ten sources whose position is within the AGN regions, but given that the CIII and/or HeII emission lines are actually limits, could move into the SF regions. We call these sources "possible AGN" and indicate them in magenta;
- twenty-nine sources whose position is consistently in the SF region for all UV-BPT diagram. We call of course these sources "SF" and indicate them in black.

We note that of the 8 X-ray detected LAGNs, 1 source is consistently located within the SF region, while the other are in the AGN region. This could be due either to a limitation of the models in reproducing all AGN properties or to the fact that in many objects the UV emission line might be of mixed origin.

4.4. Spectral stacking

To further shed light on the real nature of the ten possible AGNs we apply a spectra stacking technique to infer the average properties of these sources.

Following Saxena et al. (2020), the stacking is performed by first converting each spectrum to the rest-frame, using the spectroscopic redshift given by the DR4 catalog. We point out that the VANDELS redshifts are not the systemic ones, since they are derived by a match to spectral templates and they are driven by absorption and/or emission lines depending on their strength (Garilli et al. 2021). For this reason in the stacks the various lines might not appear at the position expected, for example the CIII is not at the exact redshift as we would expect if we had used the systemic redshift for each source. For our analysis of the stacks we neglect this effect. The rest-frame spectra are first normalized using the mean flux density value in the rest-frame wavelength range $1300\,\text{Å} < \lambda < 1500\,\text{Å}$. The spectra are then resampled to a wavelength grid ranging from 1200 to 2000 Å, with a step size of 0.582 Å (the wavelength resolution obtained at a redshift of 3.6, which is the median redshift of VANDELS sources in this work). The errors on the stacked spectra are calculated using bootstrapping: we randomly sample and stack the same number of galaxies from the sample 500 times, and the dispersion on fluxes thus obtained gives the errors (Fig. 5).

We produce three different stacks, one of the possible AGNs (ten objects), one with the certain AGNs (four sources) and one with the purely SF galaxies (twenty-nine sources). The spectra obviously reveal a wide range of emission and absorption features, with the Lyα emission line standing out in each of the sub-samples.

The main UV emission lines are fitted with a Gaussian to determine their fluxes and the CIV EW, in order to place the stacks in the various UV-BPT diagrams, an the results are presented in Fig. 6. We show just one UV-BPT them since the results are consistent for all of them: the blue star represents the sure AGNs, the magenta one the possible AGNs, and the black one the SF galaxies (in accordance with the colors used in Fig. 4). As in the previous UV-BPTs, the green dots are obtained from the AGN models from Feltre et al. (2016) and the red dots from the SF models from Xiao et al. (2018), Gutkin et al. (2016), while the grey lines are the division derived in this work and the green dashed lines refer to Nakajima et al. (2018b). We note again that the AGN stack is not well reproduced by the AGN models but rather sits in an intermediate position.

In the SF stacked spectrum (Fig. 5) we note that the HeII emission is basically unresolved ($FWHM < 600\,\text{km s}^{-1}$). This confirms the nebular nature of the HeII: in fact stellar HeII is expected to be much broader of the order of 1500–2000 km s^{-1} as seen for example in the stacks of the general LBG population (Shapley et al. 2003). For example Cassata et al. (2013) used a threshold of 1200 km s^{-1} to identify narrow HeII emitters of nebular origin. Thus, we can exclude a stellar origin for our sources.

4.5. Nature of the possible AGNs

The properties of the stacked spectra are as expected in the sense that the magenta star is at an intermediate position between the other two: however in all diagrams it is more consistent with the SF regions, indicating that the 10 sources are dominated by SF galaxies rather than AGN.

Another check on the nature of the "possible AGN" sample can be obtained by the NV emission. For AGNs, as predicted from theoretical and observational studies (e.g., Hamann & Ferland 1992, 1993; Hamann et al. 2002), we expect a bright NV line. Therefore, we determine the Lyα/NV emission line ratio for our three different stacks. For the SF galaxies stacked spectrum the NV line is not detected at all and we can place a limit Lyα/NV > 30. The stack of the possible AGN presents a Lyα/NV = 18.4 ± 0.7 that is considerably higher than the certain AGN one (Lyα/NV = 6.0 ± 0.8), although we have a 2σ detection of the NV. This value is higher than the ratios measured in narrow line AGNs (Lyα/NV ~1−2; Tilvi et al. 2016; Hu et al. 2017; Sobral et al. 2019).

We finally exploit the *Chandra* X-ray observations: although we have excluded the individually detected X-ray sources since the very beginning, the Luo et al. (2017) sources are those detected at 5σ, therefore we cannot exclude faint emission from the "possible AGN" sample. We therefore stacked the X-ray data to check if we detect any flux from the combination of the sources. Unfortunately we can do this in a meaningful way only for the 6 CDFS sources which have much deeper X-ray observations (7 Msec; Luo et al. 2017) while for the UDS field we only have much shallower observations (Kocevski et al. 2018). To stack the X-ray data we follow the same procedure described in Saxena et al. (2021). The stack does not produce any detection, although the limit is not very stringent since there are only 6 sources of which one lies at the border of the *Chandra* field.

In conclusion, from the position of the stack in the four UV-BPT diagrams, the high Lyα/NV ratio and the absence of X-ray emission in the stack, we conclude that the sample of 10 possible AGN must be dominated by SF galaxies, although we cannot exclude a (faint) AGN contribution. In the following we include these 10 sources in the SF sample, bringing it to 39 galaxies in total, to study their physical properties.

5. Physical properties of the SF CIV emitters

The combined synergy of both space-based and ground-based telescopes in the VANDELS fields provide an excellent multi-wavelength dataset from ultraviolet (UV) to mid-infrared (MIR), allowing accurate determination of the physical integrated properties of the VANDELS galaxies. We now describe the SED fitting tool that we have used to determine the physical properties, the procedure adopted and the main results.
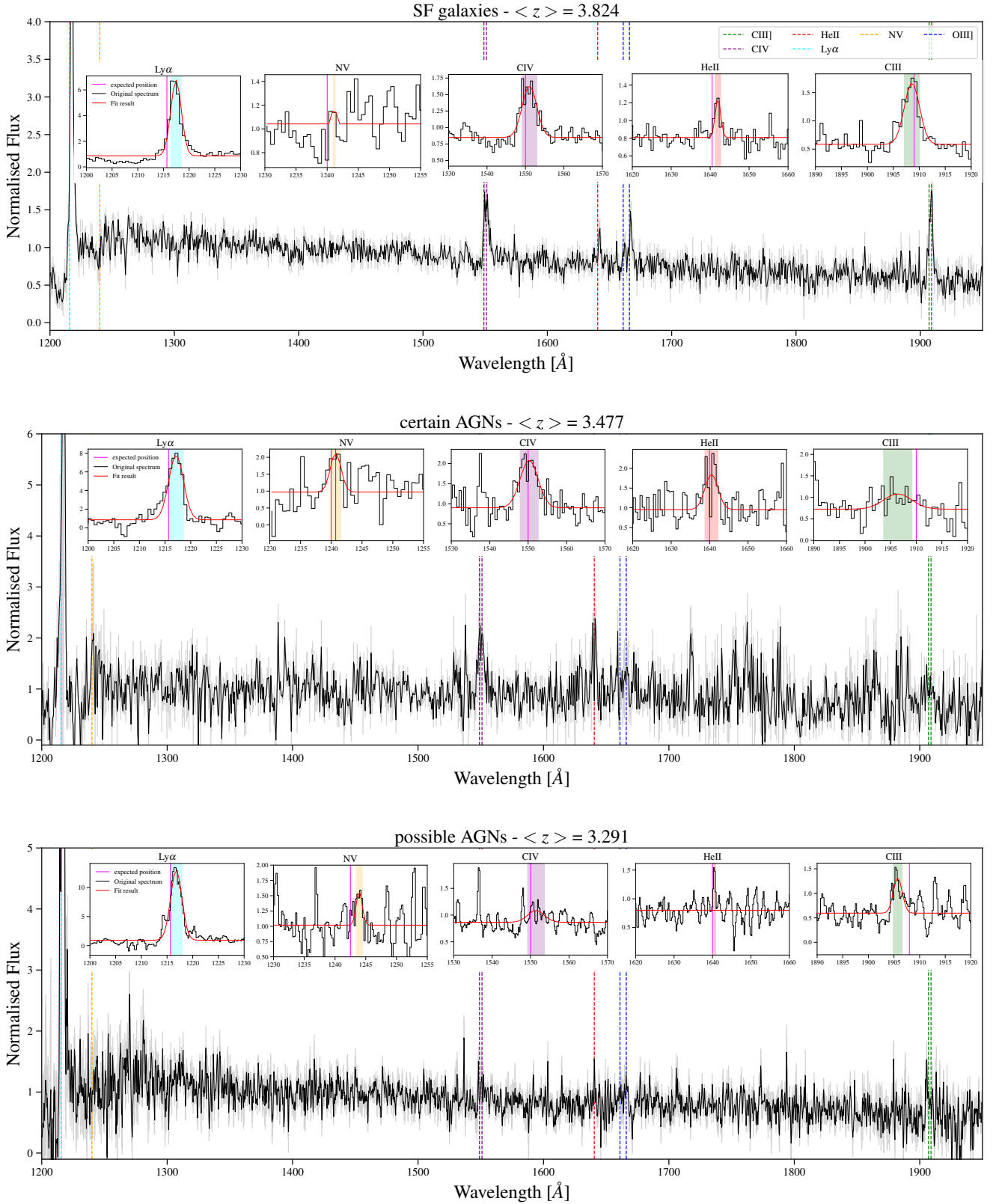
Fig. 5. Stacked spectra of the sources in our sample. Upper panel. Stacked spectrum (black) of all the 29 SF galaxies of the sample. Middle panel. Stacked spectrum of all the certain 4 AGNs of the sample (no X-ray detection). Lower panel. Stacked spectrum of all the possible 10 AGNs of the sample. The noise obtained from bootstrapping is shown in grey. For clarity, the Gaussian fits with 1 σ regions for the emission lines Lyα, Nv, Civ, HeII and CIII in each stacked spectrum considered in this work are also present. Certain and possible AGN composite show clear broad nebular emission line features in their spectra, while the SF stack show much narrower lines.

UV-BPT1
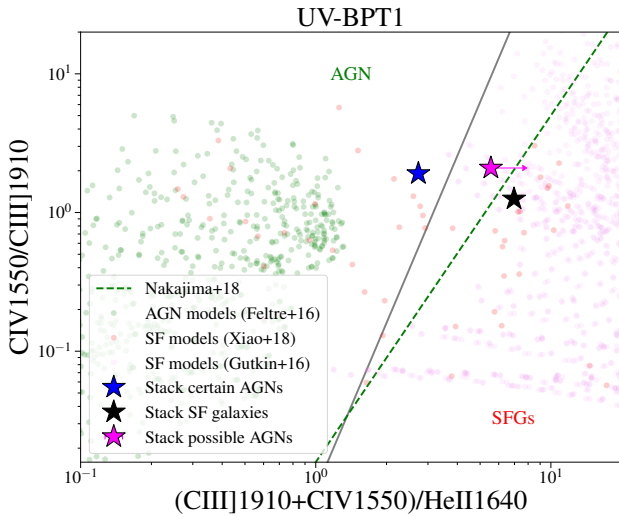
Fig. 6. UV diagnostic diagram presenting photoionization models of AGNs (Feltre et al. 2016) and SF galaxies (Gutkin et al. 2016; Xiao et al. 2018). The separating lines consistently divide the two populations and thus the results from the stack spectra for the SF galaxies, the certain AGNs and the possible AGNs (respectively the stars in black, magenta and blue).

5.1. The BEAGLE tool

The code used for the spectral energy distribution (SED) fitting is the BEAGLE (BayEsian Analysis of GaLaxy sEds) software (Chevallard & Charlot 2016) which was chosen for its versatility: through the Bruzual & Charlot libraries it allows us to model in a coherent way the continuous radiation coming from the stars of the galaxies and the nebular component which is modeled with CLOUD. The code also includes several prescriptions to describe the dust attenuation and the radiation transfer through the intergalactic medium. Stellar formation and chemical enrichment histories are included both with parametric and non parametric prescription. Finally, BEAGLE can simultaneously fit the photometry and the spectra (or individual spectral indices) of the galaxies. BEAGLE was run on all the VANDELS parent sample using v0.24.5 which employs the most recent version of the Bruzual & Charlot (2003) stellar population synthesis models (see Vidal-García et al. 2017, for details). The full description of the method and the results on the entire sample will be discussed in a companion paper (Castellano et al., in prep.). We provide here only a brief description of the most important parameters adopted: in particular we assume a delayed star formation history (SFH), which is the most flexible parametric SFH used by the code, with a current SF timescale (i.e., duration of the current episode of star formation) of 10 Million years. The escape fractions f_{esc} assumed in the BEAGLE run are set to 0 for all galaxies, regardless of the presence of the CIV emission. We used a Chabrier (2003) Initial Mass Function, metallicity in the range $-2.2 \leq \log(Z/Z_\odot) \leq 0.25$ and we treated the attenuation following the Charlot & Fall (2000) model combined with the Chevallard et al. (2013) prescriptions for geometry and inclination effects.

For each source, BEAGLE is run on the combination of photometry, coming from the official 13 band VANDELS catalog presented in Garilli et al. (2021), and spectral indices i.e., the fluxes of the HeII, OIII and CIII emission lines as well as the precise spectral windows used (respectively [1634–1654], [1663–1668] and [1897–1919]). After some tests we decided

not to provide the measured CIV emission to BEAGLE as a further spectral index to fit, both to have an unbiased estimate of the physical parameters, and also because as just discussed in Sect. 4.3, there is a well known inability of stellar population models, even when including binary stars, to reproduce some UV line fluxes (also see Saxena et al. 2022a). We also tested how the choice of current SF timescale could change our results. In particular this is relevant since the EWs of the emission lines are strongly dependant on the current SF. As a result even when reducing the SF timescale to 5 Myr, the physical parameters remain very stable with the exception of ξ_{ion}, which becomes slightly higher (~0.1 dex) for all galaxies. We note that the inferred ξ_{ion} from BEAGLE is almost independent from the initially assumed f_{esc}: this value is determined by the intrinsic ionizing SED, which is already adjusted for relatively low metallicities and young ages. The change in ξ_{ion} is substantial only for very high f_{esc} (see e.g., Marques-Chaves et al. 2022). The official VANDELS redshift was assumed in all cases for the SED fitting.

As a result, BEAGLE provides the best SED fit and the best physical parameters, with relative uncertainties: specifically total stellar mass, star formation rate, dust attenuation, age and ξ_{ion} were retrieved. For a complete list of the selected physical parameters and the range provided a priori to fit all the sources of the sample, see Table A.1 in the Appendix.

5.2. Results and comparison to parent population

Using the derived physical properties we searched for systematic differences between the SF sample of the CIV emitters (39 galaxies) and the parent sample. From the parent sample we have removed all X-ray emitters and all possible AGN as defined in Bongiorno et al. (in prep.). In Fig. 7 we present the location of our CIV emitters on the main sequence i.e., the stellar mass vs. SFR plot: given that our sample spans a rather large redshift range, we split the plot into two redshift bins, $2.7 < z \leq 4$, and $4 < z \leq 5$. The blue lines are obtained using the main sequence as a function of redshift described in Santini et al. (2017). The VANDELS sources as well as the CIV emitters sub-sample are located more or less on the main sequence of SF galaxies, with perhaps a small bias in the high redshift bin, where the (few) objects are mostly located on or above the MS.

In Fig. 8 we then show the normalized distributions of the derived stellar masses, the SFRs, the photon production efficiencies ξ_{ion} and the stellar ages of the CIV galaxies and the parent population. In each panel we also indicate the mean and median values for the two samples with vertical regions, whose widths represent the uncertainty. From the panels we can see that the CIV emitters tend to have considerable lower masses, slightly lower SFR, higher ξ_{ion} and slightly lower stellar ages compared to the parent sample. To assess the significance of these differences, we employ the common Kolmogorov-Smirnov (KS) test. From the p-values (reported in the figures) we conclude that the mass and ξ_{ion} of the CIV emitters and the parent sample are statistically different, while the max_stellar_age and the SFR are compatible with being randomly drawn. In Castellano et al. (in prep.) we find a strong link between the sSFR and ξ_{ion}: indeed if we look at our CIV emitters they have slightly higher sSFR compared to the parent population, which could explain the higher ξ_{ion}. This link and its implications will further discussed in that paper. Even using a SF timescale of 5 Myrs, with all values of ξ_{ion} being slightly higher, the difference between CIV emitters and the parent sample is still significant.
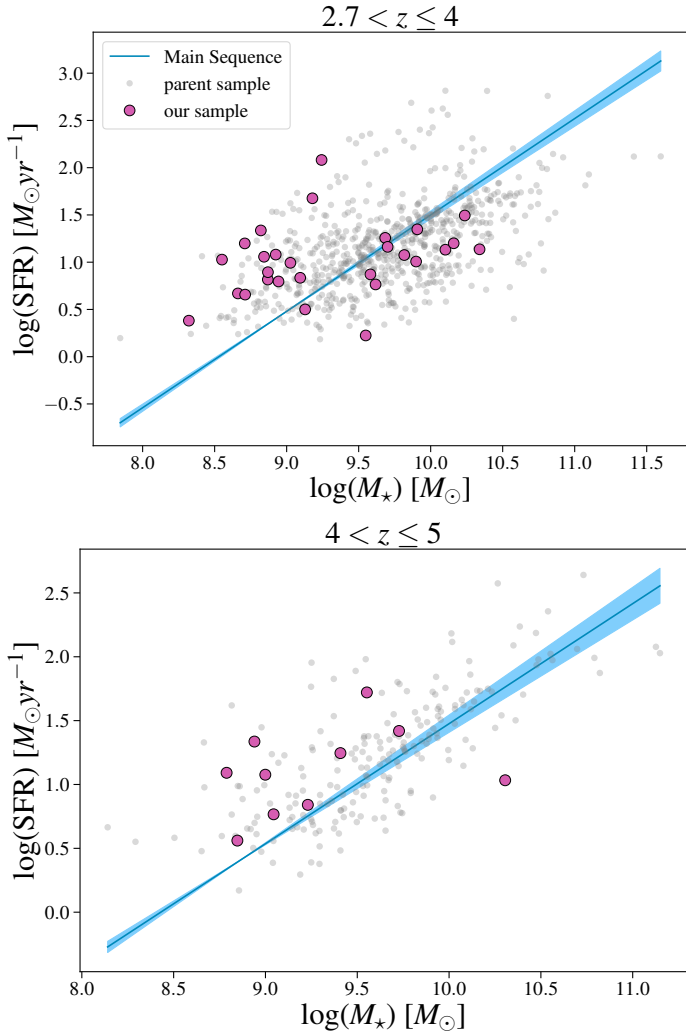
Fig. 7. Stellar mass vs. SFR relation for our CIV emitters (purple dots) and the parent sample (grey dots). The blue line shows the main sequence respectively at $3 < z \leq 4$, $4 < z \leq 5$ from Santini et al. (2017).

In conclusion our CIV emitters are in general low mass objects which have an higher photon production rate compared to the general SF population at the same redshift.

5.3. Average stellar metallicity

The link between the presence of nebular CIV emission and low metallicity stellar population has been noted both at high and low redshift. For example Senchyna et al. (2017) showed that CIV emission may be ubiquitous in extremely metal-poor galaxies with very high specific star formation rates, although it reaches large EWs only if the ISM is exposed to the hard stellar ionizing spectra produced at extremely low metallicities ($12 + \log O/H \lesssim 7.7$).

To derive the stellar metallicity from our spectra, we use the method developed by Calabrò et al. (2021), which is based on stellar photospheric absorption features at 1501 Å and 1719 Å, calibrated with Starburst99 models and are largely unaffected by stellar age, dust, IMF, nebular continuum, or interstellar absorption. The method can be applied to spectra with a S/N of 15–20 in the continuum to avoid large uncertainty, and therefore we cannot derive metallicities for individual sources but only aver-
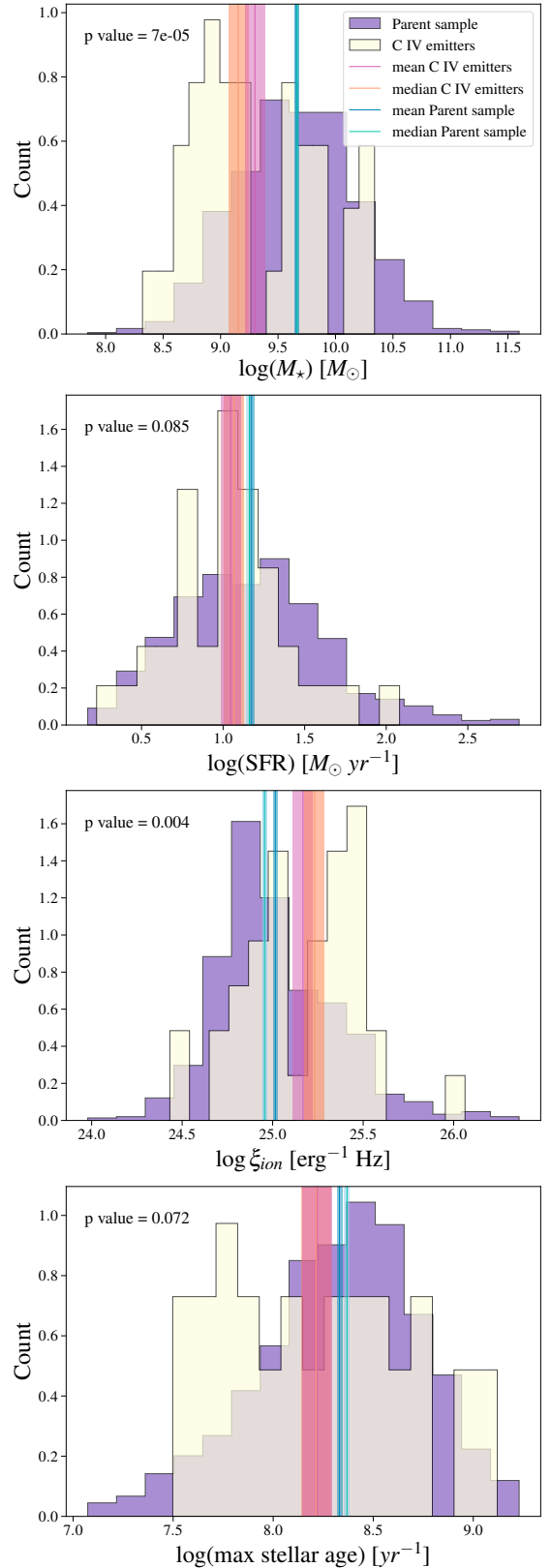
Fig. 8. Derived stellar mass, SFR, ionizing photon production efficiency ξ_{ion} and stellar age of the sources identified as SF, determined by BEAGLE (light distribution). For comparison, those of the total sample in the same redshift range are also shown in the figure (purple distribution). The figure also shows the mean and median with their standard deviations for the distributions and the p-value from the KS test for the main physical properties of the analyzed sample.
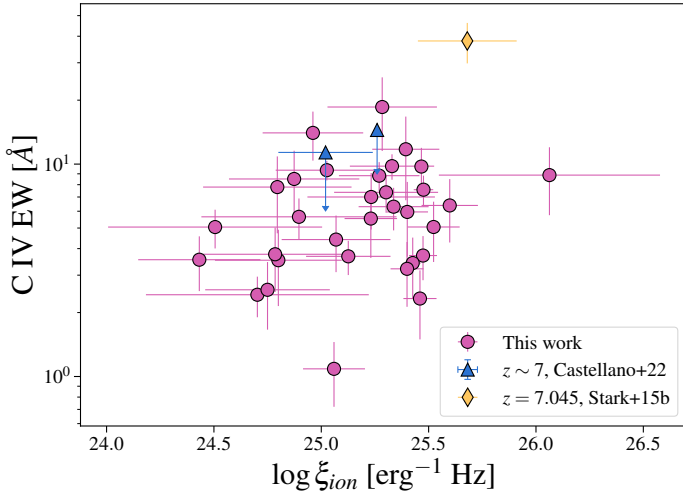
Fig. 9. Distribution of the measured EW(CIV) and the ξ_{ion} for the selected SF galaxies identified in both CDFS and UDS fields (purple points) compared with $z \sim 7$ objects from literature: Castellano et al. (2022; blue points) and Stark et al. (2015; orange point).

age values from stacked spectra. We produced a stack of the 39 SF galaxies following the procedure outlined in the previous section. The metallicity we derive is $Z \sim 0.26 Z_\odot$ for the sample of 29 purely SF galaxies and a slightly lower (but consistent within the uncertainties) value of $Z \sim 0.1 Z_\odot$ for the combined sample of 39 galaxies. Looking at the stellar mass-stellar metallicity relation by Calabrò et al. (2021) we can see that these low metallicities (about $0.15 Z_\odot$) are perfectly consistent with the general trend for $z \sim 3$ galaxies with similar masses, i.e., the CIV emitting galaxies do not show lower metallicities compared to their parent sample, as also found by Saxena et al. (2022a). This is therefore at odds with the low redshift universe where CIV emitters have almost always an inferred stellar (and gas phase) metallicities are extremely low (e.g., Berg et al. 2019; Senchyna et al. 2021). However in terms of "absolute" metallicity, $z \sim 3$ CIV emitters have a similar metallicity as the local universe emitters: this is of course due to the fact that at $z \sim 3.5$ the average metallicity of SF galaxies is a factor of 0.6 dex lower than in the local universe (Cullen et al. 2019; Calabrò et al. 2021).

6. Discussion: The ionizing properties of CIV emitters

In the previous sections we have found that the VANDELS CIV emitters are in general galaxies with low masses and high photon production efficiency compared to their parent population. They have stellar metallicities of $0.1-0.15 Z_\odot$ consistent with the stellar-mass stellar metallicity relation at redshift 3.5. Most of our CIV emitters show also a prominent Lyα emission, and we observe a strong correlation between the CIV and the Lyα flux (shown in Fig. 3). We now investigate if the CIV emitters have properties that could make them potentially good ionizers.

An investigation of ionizing efficiency is the first step in identifying good candidates for cosmic reionizers. Photon production efficiency expectations depend on several factors, including the initial mass function, the SFH, the evolution of individual stars, the stellar metallicity, and potential binary interactions between stars (e.g., Zackrisson et al. 2011, 2013, 2017;

Eldridge et al. 2017; Stanway & Eldridge 2018, 2019), but they agree in identifying the expected value of $\log \xi_{ion}$ around 25.3 to ionize the IGM at $z > 6$ (Robertson et al. 2013, 2015). This prediction is confirmed both from the local universe and intermediate and high redshifts' observations (e.g., Stark et al. 2015, 2017; Bouwens et al. 2016; Matthee et al. 2017; Izotov et al. 2017; Nakajima et al. 2018a; Shivaei et al. 2018; Lam et al. 2019; Atek et al. 2022; Castellano et al. 2022). $\log \xi_{ion}$ is also known to have a higher-than-average value when strong Lyα (e.g., Harikane et al. 2018; Sobral & Matthee 2019; Cullen et al. 2019) and UV-rest frame emission lines (e.g., Nakajima et al. 2016; Tang et al. 2019) are present. Using the results obtained from our sample, we examine the dependence of the $\log \xi_{ion}$ (calculated, as stated in Sect. 5.2, without considering CIV emission) with respect to the EW$_0$ of the nebular CIV. The results are shown in Fig. 9. We also compare our values with $z \sim 7$ objects from literature (Stark et al. 2015; Castellano et al. 2022) with CIV detection. According to this analysis, high CIV emission would be accompanied by an increase in ξ_{ion} values, which are also within the range expected for cosmic reionization. For a detailed examination of ξ_{ion} in relation to the VANDELS sample proprieties, see Castellano et al. (in prep.).

We now turn to the other relevant necessary condition for an ionizer, i.e., the LyC escape fraction. We know that the presence of strong Lyα emission is tightly linked to the escape of LyC photons. Galaxies with moderate values of f_{esc} are in general characterized by strong Lyα emission, as observed both in individually detected galaxies (e.g., Gazagnes et al. 2020; Pahl et al. 2021; Begley et al. 2022; Flury et al. 2022b, at high and low redshifts, respectively) and via stacked spectroscopic studies (e.g., Marchi et al. 2018; Steidel et al. 2018). Such a tight relation is also predicted by models which show that both ionizing continuum flux and Lyα photons can escape through the same ionized channels in the interstellar medium (Rivera-Thorsen et al. 2015, 2017; Verhamme et al. 2015, 2017; Dijkstra et al. 2016; Steidel et al. 2018; Marchi et al. 2018; Izotov et al. 2020, 2021; Gazagnes et al. 2020). We checked the 37 VANDELS CIV emitters that have their Lyα in the observed spectral range (all those at $z > 3$), and only one has Lyα in absorption, while 24 have Lyα EW larger than 20 Å, with several above 100 Å. This would imply that a good fraction of the CIV emitters might also be galaxies with non negligible ionizing escape fractions. As shown by Verhamme et al. (2017), the Lyα profiles of strong LyC leakers are in general all double-peaked with a small peak separation, in agreement with our theoretical expectation: unfortunately due to the relatively low resolution of the VANDELS spectra we are not able to determine if this is also the case for our CIV emitters.

We further checked whether the properties of our CIV emitters are similar to the LyC leakers of Schaerer et al. (2022). They define strong leakers as those galaxies with a LyC escape fraction above 10% (i.e., $f_{esc} > 0.1$) and found that these galaxies show not only the presence of CIV emission but also a high ratio, C43 = CIV/CIII] > 0.75.

In Fig. 10 we show the C43 values for our sample, in the cases when the CIII] emission is measurable (in 10 out of 39 cases, the CIII] falls outside the range included in the VANDELS spectra). For 22 galaxies the C43 ratio is clearly > 0.75 and only in 4 cases it is smaller, with the rest being galaxies in which the relatively high CIII] limit prevents us from drawing any conclusion. In any case at least two thirds of the CIV emitters seem to have properties consistent with the low redshift LyC leakers presented in Schaerer et al. (2022). Since in

Schaerer et al. (2022) the CIV emission was purely nebular in origin, in this figure we also show how the results would be effected by considering the possible stellar contribution. The grey symbols in Fig. 10 thus represent the effect of assuming a 20% stellar contribution correction on the sample. We note that only two sources move outside the previously defined leakers' region, but given the high uncertainties on C43, the basic conclusions remain unchanged.

In a companion paper (Saxena et al. 2022a) we have investigated a sub-sample of the bright VANDELS CIV emitters by means of spectral stacking to understand if they could indeed be good tracers of hydrogen ionizing LyC photon leakage using a variety of indicators. We found that equivalent width and offset of the Lyα peak from the systemic redshift of galaxies is indicative of significant LyC leakage. These characteristics are consistent with the predictions of e.g. Dijkstra (2014) and Verhamme et al. (2015) of high Lyα and LyC escape in galaxies. In addition, the depth and velocity offsets of low-ionization interstellar absorption features in the stack, are indicative of low column density channels through which LyC photons may escape (e.g., Chisholm et al. 2020; Saldana-Lopez et al. 2022b), with their low covering fractions suggesting LyC $f_{esc} \simeq 0.05 - 0.30$.

In conclusion, a consistent picture emerges, in this work and in the parallel analysis by Saxena et al. (2022a) in that a substantial fraction of galaxies showing nebular CIV emission, could be galaxies with significant production and escape of LyC photons. They could therefore be the best analogs of those galaxies that mostly contributed to cosmic reionization at $z > 7$. We have shown that CIV emitters do not differ significantly from low-mass galaxies apart from enhanced ξ_{ion} (which is probably insufficient to explain the strong UV emission lines associated with CIV). So if the integrated properties (SFR, metallicity, etc.) are equal, the intense UV emission must be instead linked to a peculiar ISM structure. For example, it has been shown that in order to accurately reproduce such high UV emission lines, gas-denser regions and lower-density regions must have different ionizations (Berg et al. 2021; Schaerer et al. 2022) in order to facilitate the escape of ionizing photons. The Lyα flux at systemic velocity (Saxena et al. 2022b) observed in the stack of the bright CIV emitters supports this scenario, suggesting that it is the ISM properties that make the CIV emitting galaxies different from the parent population.

Finally, we identify the best candidate ionizers in our sample by selecting all galaxies having C43 = CIV/CIII] > 0.75, EW(Lyα)>20 Å, and $\xi_{ion} > 25$ (the median of the parent sample): in total we have 12 sources with these combined properties and we indicate them in red in Table 1. Note that Lyα and CIII] are outside of the observed range respectively for 2 and 10 of the SF sample, so the 12 candidates are selected from a usable sample of only 31 galaxies, thus representing almost 40% of the galaxies.

7. Summary and conclusions

In this paper we have presented a detailed investigation of SF galaxies at $2.5 \leq z \leq 5$ which show significant nebular CIV emission, drawn from the VANDELS survey (McLure et al. 2018; Pentericci et al. 2018a). We summarize our findings as follows:

1. At $2.5 \leq z \leq 5$, CIV emitters represent just ~4% of the VANDELS SF population (933 sources). Their EW_0s range from 1 to 29 Å (Sect. 3). The CIV strength correlates well with the strength of the other UV emission lines.
2. Using the UV-BPTs diagrams, we have identified those sources that are powered by stellar photoionization, indi-
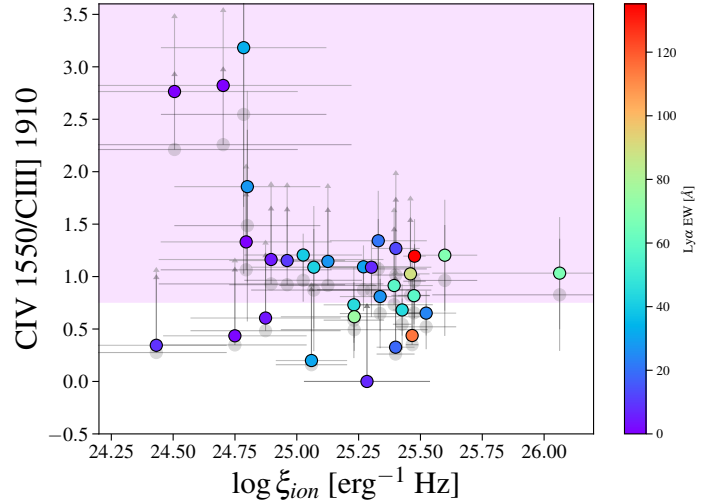
Fig. 10. Ratio of CIV and CIII] versus the ξ_{ion} for individual galaxies in this study. The shaded area limits C34 > 0.75, that was empirically suggested by Schaerer et al. (2022) to host strong LyC emitting galaxies ($f_{esc} > 0.1$). The sources are colored using the Lyα EW values. We find that 21 out of 32 galaxies in our sub-sample have CIV/CIII] ratios > 0.75. In grey we plot the same population assuming an average stellar correction of 20%.

cating massive stars as the only ionization source (Sect. 4), opposed to an AGN origin. Out of the 43 initially selected CIV emitters, only 4 are consistently found in the AGN region of the diagrams. For 10 sources which could possible be AGN, we resort to spectral stacking analysis and confirm that are most probably SF galaxies, bringing the final sample to 39 sources.
3. Using BEAGLE (Chevallard & Charlot 2016), by fitting photometry and the spectral indices we derived the physical properties of the SF CIV emitters (total stellar mass, SFR, ξ_{ion}, stellar age). We also derive their average stellar metallicity following Calabrò et al. (2021) method based on weak absorption lines. We find that CIV emitters are low-mass galaxies residing on the main sequence. Their metallicity is consistent with the general SF population at the same redshift, and similar to the metallicity of CIV in the local universe. CIV emitters have on average similar integrated physical properties when compared to galaxies with no CIV emission at $2.5 \leq z \leq 5$, with the exception of a higher ξ_{ion} average value.
4. Besides having high production of ionizing photons, there are several indications that CIV emitters have also high escape fractions of LyC photons: this includes the presence of bright Lyα emission and a high CIV/CIII] ratio which was recently proposed as one of the most promising indicators of a possible LyC leakage by Schaerer et al. (2022). In Sect. 6, we identify 12 galaxies as the best analogs to cosmic reionizers, showing the combination of high $\xi_{ion} > 25$, and EW(Lyα)>20 Å and CIV/CIII] > 0.75, indicative of high LyC escape fraction.

Amongst the inferred properties, the most uncertain is obviously the escape fraction: in this study we only have presented indirect evidence that the galaxies could have high f_{esc}. Unfortunately, the ultra deep VANDELS spectra only start at 4800 Å, which means that a direct measurement of the LyC flux is impossible with current data. However, at this redshift it is possible to detect the LyC flux at ~3800–4000 Å using blue-sensitive

facilities. Currently this is possible with MODS on LBT, but in the near future the upgraded FORS2 on VLT operating from 3400 Å (Boffin et al. 2020), will also be an ideal instrument. We plan therefore to validate our conclusion by observing and possibly directly detecting the LyC emission in our galaxies, and we have already been awarded time on the LBT to follow up the UDS sources. If we indeed confirm that CIV emitters are good ionizers, having both high photon production and high escape fraction, this could have important implications to understand the epoch of reionization, where obviously the LyC flux is not observable directly: indeed Lyα, one of the best indirect indicators of LyC escape, looses visibility when the IGM starts to be highly neutral, as it is easily suppressed by neutral hydrogen and is visible only in highly ionized peculiar regions (Castellano et al. 2022). Nebular CIV emission on the other hand would be easily observable with JWST/NIRSpec in SF galaxies up to very high redshift and could therefore be used as a valid alternative to pinpoint the sources responsible for cosmic reionization.

References

Amorín, R., Fontana, A., Pérez-Montero, E., et al. 2017, Nat. Astron., 1, 0052
Astropy Collaboration (Price-Whelan, A. M., et al.) 2018, AJ, 156, 123
Atek, H., Furtak, L. J., Oesch, P., et al. 2022, MNRAS, 511, 4464
Baldwin, J. A., Phillips, M. M., & Terlevich, R. 1981, PASP, 93, 5
Begley, R., Cullen, F., McLure, R. J., et al. 2022, MNRAS, 513, 3510
Berg, D. A., Chisholm, J., Erb, D. K., et al. 2019, ApJ, 878, L3
Berg, D. A., Chisholm, J., Erb, D. K., et al. 2021, ApJ, 922, 170
Boffin, H. M. J., Dérie, F., Manescau, A., et al. 2020, SPIE Conf. Ser., 11447, 114477A
Bolan, P., Lemaux, B. C., Mason, C., et al. 2022, MNRAS, 517, 3263
Bouwens, R. J., Smit, R., Labbé, I., et al. 2016, ApJ, 831, 176
Brammer, G. B., van Dokkum, P. G., & Coppi, P. 2008, ApJ, 686, 1503
Bruzual, G., & Charlot, S. 2003, MNRAS, 344, 1000
Caffau, E., Ludwig, H. G., Steffen, M., Freytag, B., & Bonifacio, P. 2011, Sol. Phys., 268, 255
Calabrò, A., Castellano, M., Pentericci, L., et al. 2021, A&A, 646, A39
Calzetti, D., Armus, L., Bohlin, R. C., et al. 2000, ApJ, 533, 682
Cassata, P., Le Fèvre, O., Charlot, S., et al. 2013, A&A, 556, A68
Castellano, M., Pentericci, L., Cupani, G., et al. 2022, A&A, 662, A115
Chabrier, G. 2003, PASP, 115, 763
Charlot, S., & Fall, S. M. 2000, ApJ, 539, 718
Chevallard, J., & Charlot, S. 2016, MNRAS, 462, 1415
Chevallard, J., Charlot, S., Wandelt, B., & Wild, V. 2013, MNRAS, 432, 2061
Chisholm, J., Prochaska, J. X., Schaerer, D., Gazagnes, S., & Henry, A. 2020, MNRAS, 498, 2554
Cullen, F., McLure, R. J., Dunlop, J. S., et al. 2019, MNRAS, 487, 2038
Dijkstra, M. 2014, PASA, 31, e040
Dijkstra, M., Gronke, M., & Venkatesan, A. 2016, ApJ, 828, 71
Du, X., Shapley, A. E., Tang, M., et al. 2020, ApJ, 890, 65
Eldridge, J. J., Stanway, E. R., Xiao, L., et al. 2017, PASA, 34, e058
Feltre, A., Charlot, S., & Gutkin, J. 2016, MNRAS, 456, 3354
Ferland, G. J., Porter, R. L., van Hoof, P. A. M., et al. 2013, Rev. Mex. Astron. Astrofis., 49, 137
Flury, S. R., Jaskot, A. E., Ferguson, H. C., et al. 2022a, ApJ, 930, 126
Flury, S. R., Jaskot, A. E., Ferguson, H. C., et al. 2022b, ApJS, 260, 1
Garilli, B., Fumana, M., Franzetti, P., et al. 2010, PASP, 122, 827
Garilli, B., Paioro, L., Scodeggio, M., et al. 2012, PASP, 124, 1232

Garilli, B., McLure, R., Pentericci, L., et al. 2021, A&A, 647, A150
Gazagnes, S., Chisholm, J., Schaerer, D., Verhamme, A., & Izotov, Y. 2020, A&A, 639, A85
Grogin, N. A., Kocevski, D. D., Faber, S. M., et al. 2011, ApJS, 197, 35
Groves, B. A., Dopita, M. A., & Sutherland, R. S. 2004, ApJS, 153, 75
Gutkin, J., Charlot, S., & Bruzual, G. 2016, MNRAS, 462, 1757
Hamann, F., & Ferland, G. 1992, ApJ, 391, L53
Hamann, F., & Ferland, G. 1993, ApJ, 418, 11
Hamann, F., Korista, K. T., Ferland, G. J., Warner, C., & Baldwin, J. 2002, ApJ, 564, 592
Harikane, Y., Ouchi, M., Shibuya, T., et al. 2018, ApJ, 859, 84
Harris, C. R., Millman, K. J., van der Walt, S. J., et al. 2020, Nature, 585, 357
Hu, W., Wang, J., Zheng, Z.-Y., et al. 2017, ApJ, 845, L16
Hunter, J. D. 2007, Comput. Sci. Eng., 9, 90
Inoue, A. K., Shimizu, I., Iwata, I., & Tanaka, M. 2014, MNRAS, 442, 1805
Isobe, T., Feigelson, E. D., & Nelson, P. I. 1986, ApJ, 306, 490
Izotov, Y. I., Guseva, N. G., Fricke, K. J., Henkel, C., & Schaerer, D. 2017, MNRAS, 467, 4118
Izotov, Y. I., Worseck, G., Schaerer, D., et al. 2018, MNRAS, 478, 4851
Izotov, Y. I., Schaerer, D., Worseck, G., et al. 2020, MNRAS, 491, 468
Izotov, Y. I., Worseck, G., Schaerer, D., et al. 2021, MNRAS, 503, 1734
Jung, I., Finkelstein, S. L., Dickinson, M., et al. 2020, ApJ, 904, 144
Kocevski, D. D., Hasinger, G., Brightman, M., et al. 2018, ApJS, 236, 48
Koekemoer, A. M., Faber, S. M., Ferguson, H. C., et al. 2011, ApJS, 197, 36
Kriek, M., van Dokkum, P. G., Labbé, I., et al. 2009, ApJ, 700, 221
Lam, D., Bouwens, R. J., Labbé, I., et al. 2019, A&A, 627, A164
Le Fèvre, O., Lemaux, B. C., Nakajima, K., et al. 2019, A&A, 625, A51
LLerena, M., Amorín, R., Cullen, F., et al. 2022, A&A, 659, A16
Luo, B., Brandt, W. N., Xue, Y. Q., et al. 2017, ApJS, 228, 2
Mainali, R., Kollmeier, J. A., Stark, D. P., et al. 2017, ApJ, 836, L14
Mainali, R., Zitrin, A., Stark, D. P., et al. 2018, MNRAS, 479, 1180
Marchi, F., Pentericci, L., Guaita, L., et al. 2018, A&A, 614, A11
Marchi, F., Pentericci, L., Guaita, L., et al. 2019, A&A, 631, A19
Marques-Chaves, R., Schaerer, D., Álvarez-Márquez, J., et al. 2022, MNRAS, 517, 2972
Matthee, J., Sobral, D., Best, P., et al. 2017, MNRAS, 465, 3637
McLure, R. J., Pentericci, L., Cimatti, A., et al. 2018, MNRAS, 479, 25
Nagao, T., Maiolino, R., & Marconi, A. 2006, A&A, 459, 85
Naidu, R. P., Matthee, J., Oesch, P. A., et al. 2022, MNRAS, 510, 4582
Nakajima, K., Ellis, R. S., Iwata, I., et al. 2016, ApJ, 831, L9
Nakajima, K., Fletcher, T., Ellis, R. S., Robertson, B. E., & Iwata, I. 2018a, MNRAS, 477, 2098
Nakajima, K., Schaerer, D., Le Fèvre, O., et al. 2018b, A&A, 612, A94
Nanayakkara, T., Brinchmann, J., Boogaard, L., et al. 2019, A&A, 624, A89
Oke, J. B., & Gunn, J. E. 1983, ApJ, 266, 713
Ouchi, M., Ono, Y., & Shibuya, T. 2020, ARA&A, 58, 617
Pahl, A. J., Shapley, A., Steidel, C. C., Chen, Y., & Reddy, N. A. 2021, MNRAS, 505, 2447
Pentericci, L., McLure, R. J., Garilli, B., et al. 2018a, A&A, 616, A174
Pentericci, L., Vanzella, E., Castellano, M., et al. 2018b, A&A, 619, A147
Planck Collaboration XIII. 2016, A&A, 594, A13
Rivera-Thorsen, T. E., Hayes, M., Östlin, G., et al. 2015, ApJ, 805, 14
Rivera-Thorsen, T. E., Dahle, H., Gronke, M., et al. 2017, A&A, 608, L4
Robertson, B. E. 2022, ARA&A, 60, 121
Robertson, B. E., Schneider, E., Ellis, R. S., et al. 2013, Am. Astron. Soc. Meeting Abstr., 221, 207.02
Robertson, B. E., Ellis, R. S., Furlanetto, S. R., & Dunlop, J. S. 2015, ApJ, 802, L19
Saldana-Lopez, A., Schaerer, D., Chisholm, J., et al. 2022a, MNRAS, 522, 6295
Saldana-Lopez, A., Schaerer, D., Chisholm, J., et al. 2022b, A&A, 663, A59
Santini, P., Fontana, A., Castellano, M., et al. 2017, ApJ, 847, 76
Saxena, A., Pentericci, L., Mirabelli, M., et al. 2020, A&A, 636, A47
Saxena, A., Ellis, R. S., Förster, P. U., et al. 2021, MNRAS, 505, 4798
Saxena, A., Cryer, E., Ellis, R. S., et al. 2022a, MNRAS, 517, 1098
Saxena, A., Pentericci, L., Ellis, R. S., et al. 2022b, MNRAS, 511, 120
Schaerer, D., Izotov, Y. I., Worseck, G., et al. 2022, A&A, 658, L11
Schmidt, K. B., Kerutt, J., Wisotzki, L., et al. 2021, A&A, 654, A80
Schreiber, C., Glazebrook, K., Nanayakkara, T., et al. 2018, A&A, 618, A85
Senchyna, P., Stark, D. P., Vidal-García, A., et al. 2017, MNRAS, 472, 2608
Senchyna, P., Stark, D. P., Charlot, S., et al. 2021, MNRAS, 503, 6112
Senchyna, P., Stark, D. P., Charlot, S., et al. 2022, ApJ, 930, 105
Shapley, A. E., Steidel, C. C., Pettini, M., & Adelberger, K. L. 2003, ApJ, 588, 65
Shivaei, I., Reddy, N. A., Siana, B., et al. 2018, ApJ, 855, 42
Sobral, D., & Matthee, J. 2019, A&A, 623, A157
Sobral, D., Matthee, J., Brammer, G., et al. 2019, MNRAS, 482, 2422
Stanway, E. R., & Eldridge, J. J. 2018, MNRAS, 479, 75
Stanway, E. R., & Eldridge, J. J. 2019, A&A, 621, A105

Stanway, E. R., Eldridge, J. J., & Becker, G. D. 2016, MNRAS, 456, 485
Stark, D. P., Richard, J., Siana, B., et al. 2014, MNRAS, 445, 3200
Stark, D. P., Walth, G., Charlot, S., et al. 2015, MNRAS, 454, 1393
Stark, D. P., Ellis, R. S., Charlot, S., et al. 2017, MNRAS, 464, 469
Steidel, C. C., Bogosavljević, M., Shapley, A. E., et al. 2018, ApJ, 869, 123
Talia, M., & Schreiber, C. 2023, A&A, submitted
Tang, M., Stark, D. P., Chevallard, J., & Charlot, S. 2019, MNRAS, 489, 2572
Tang, M., Stark, D. P., Chevallard, J., et al. 2021, MNRAS, 503, 4105
Tilvi, V., Pirzkal, N., Malhotra, S., et al. 2016, ApJ, 827, L14
Vanzella, E., de Barros, S., Vasei, K., et al. 2016, ApJ, 825, 41

Vanzella, E., Caminha, G. B., Calura, F., et al. 2020, MNRAS, 491, 1093
Vanzella, E., Caminha, G. B., Rosati, P., et al. 2021, A&A, 646, A57
Verhamme, A., Orlitová, I., Schaerer, D., & Hayes, M. 2015, A&A, 578, A7
Verhamme, A., Orlitová, I., Schaerer, D., et al. 2017, A&A, 597, A13
Vidal-García, A., Charlot, S., Bruzual, G., & Hubeny, I. 2017, MNRAS, 470, 3532
Xiao, L., Stanway, E. R., & Eldridge, J. J. 2018, MNRAS, 477, 904
Zackrisson, E., Rydberg, C.-E., Schaerer, D., Östlin, G., & Tuli, M. 2011, ApJ, 740, 13
Zackrisson, E., Inoue, A. K., & Jensen, H. 2013, ApJ, 777, 39
Zackrisson, E., Binggeli, C., Finlator, K., et al. 2017, ApJ, 836, 78

Appendix A: BEAGLE parameters

Table A.1. Set of BEAGLE parameters used to fit both the parent and the Civ samples' sources.

Parameter	type	info	range
sfh_type	fixed	value: delayed	
tau	fitted		[7.0, 10.5]
mass	fitted		[7.0, 12.0]
max_stellar_age	fitted		[7.0, 10.0]
formation_redshift	fitted		[7.011499, 50.0]
metallicity	fitted		[-2.2, 0.25]
sfr	fitted		[0.0, 3.0]
current_sfr_timescale	fixed	value: 7.0	
redshift	fitted		
attenuation_type	fixed	value: CF00	
tauV_eff	fitted		[0.001, 5.01]
mu	fixed	value: 0.4	
nebular_logU	fitted		[-4.0, -1.0]
nebular_xi	fitted		[0.1, 0.5]
nebular_Z	dependent		
nebular_sigma	fixed	value: 22.93	